

# Robustness of Parameter Estimation Procedures for Bulk-Heterojunction Organic Solar Cells

Alexis Prel,<sup>1</sup> Abir Rezgui,<sup>2</sup> Anne-Sophie Cordan,<sup>1</sup> and Yann Leroy<sup>1, a)</sup>

<sup>1</sup>ICube Laboratory, CNRS/Université de Strasbourg, Télécom Physique Strasbourg, Illkirch, France.

<sup>2</sup>ESYCOM, CNRS/Université Gustave Eiffel, ESIEE Paris, Marne-la-Vallée, France.

(Dated: June 8, 2021)

Parameter estimation procedures provide valuable guidance in the understanding and improvement of organic solar cells and other devices. They often rely on one-dimensional models, but in the case of bulk-heterojunction (BHJ) designs, it is not straightforward that these models' parameters have a consistent physical interpretation. Indeed, contrarily to two- or three-dimensional models, the BHJ morphology is not explicitly described in one-dimensional models and must be implicitly expressed through effective parameters. In order to inform experimental decisions, a helpful parameter estimation method must establish that one can correctly interpret the provided parameters. However, only a few works have been undertaken to reach that objective in the context of BHJ organic solar cells. In this work, a realistic two-dimensional model of BHJ solar cells is used to investigate the behavior of state-of-the-art parameter estimation procedures in situations that emulate experimental conditions. We demonstrate that fitting solely current-voltage characteristics by an effective medium one-dimensional model can yield nonsensical results, which may lead to counter-productive decisions about future design choices. In agreement with previously published literature, we explicitly demonstrate that fitting several characterization results together can drastically improve the robustness of the parameter estimation. Based on a detailed analysis of parameter estimation results, a set of recommendations is formulated to avoid the most problematic pitfalls and increase awareness about the limitations that cannot be circumvented.

Keywords: Organic Solar Cells, Bulk Hetero-Junction, Bayesian, Parameter estimation

## I. INTRODUCTION

The world's renewable energy consumption is projected to keep on rising during the upcoming decades.<sup>1,2</sup> Among other means of production that could help supply that demand, Organic Solar Cells (OSC) are a promising technology, but their power conversion efficiency remains lower than competing technologies.<sup>3</sup>

One of the most widespread strategies to improve OSC performances is the so-called bulk-heterojunction (BHJ) architecture for the active layer. In a BHJ, a donor and acceptor materials are finely mixed to form bicontinuous percolation pathways for free carriers, as depicted in Fig. 1a. Such a complicated morphology is difficult to probe with traditional investigation tools. Therefore, to further improve BHJ devices, experimental exploration would benefit from reliable modeling insight that can operate on a reasonable computational budget and explain the inner optoelectronic device processes that are hard to probe directly. To this end, parameter estimation is a helpful diagnostic tool to interpret routine device measurements.<sup>4</sup>

However, BHJ geometries are more challenging to model than a planar stack of layers. In theory, one should model the entire three-dimensional (3D) morphology and account for the influence of tortuous conduction pathways on transport to reproduce experimental observations.<sup>5</sup> In practice, detailed information at the relevant

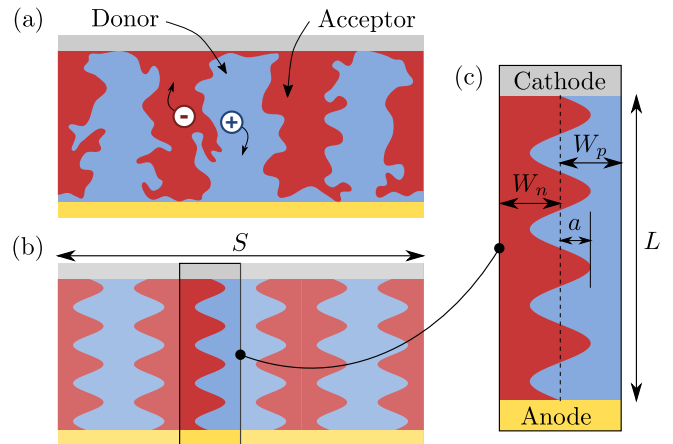


Figure 1. a) Complex percolation pathways observed in actual BHJ architecture; b) Model percolation pathways. Their tortuosity are controlled by a sinusoidal interface. The active area  $S$  is reduced to an elementary structure, repeated using mirroring boundary conditions; c) Parameters of the elementary structure considered for the simulations: active layer thickness  $L$ , half-widths of the material pathways  $W_{n,p}$ , and amplitude  $a$  of the sinus interface made of  $N_{\text{per}}$  periods.

length-scale ( $\approx 10$  nm) is seldom available. As a result, it is often argued that the active layer can be modeled as a one-dimensional (1D) effective medium with uniform physical properties, which result from a combination of the characteristics of the two considered materials and the BHJ morphology itself.<sup>6,7</sup> While it may be possible to carefully design 1D models to match the predic-

<sup>a)</sup>Correspondence to: [yann.leroy@unistra.fr](mailto:yann.leroy@unistra.fr)

tions of a more realistic model,<sup>8</sup> the physical properties of the effective medium are typically chosen to match the current-voltage (I-V) response of a fabricated device,<sup>5,9–11</sup> which can lead to arbitrary values that are not reliable.<sup>5,12,13</sup> However, it is highly desirable for the fit parameters to predict measurements not exploited during inference, identify performance bottlenecks, or otherwise suggest appropriate experiments to try next.<sup>12</sup> This work presents pieces of evidence, through numerical studies, that challenge the value of a 1D effective medium model to reach these goals.

As of today, the most realistic models such as master equation,<sup>14,15</sup> kinetic Monte Carlo,<sup>5,16,17</sup> or molecular dynamics approaches,<sup>18</sup> are prohibitively expensive for model-intensive applications such as parameter estimation<sup>13,19</sup> or machine-learning.<sup>20</sup> In contrast, fitting is often performed via equivalent circuit analysis<sup>21,22</sup> using various algorithms,<sup>23,24</sup> but the parameters derived in this way are difficult to relate to the internal physics of the active layer. Here, we focus on drift-diffusion models, as they offer a good compromise between the granularity of the description and the computation time required for simulations,<sup>25</sup> while keeping parameters with physical meanings.

With this kind of model, existing fitting approaches provide reasonable parameter values when applied to experimental measurements. However, the values are not guaranteed to be relevant if they describe a 1D effective medium model,<sup>5,9–11</sup> nor unique if obtained by local optimization.<sup>19</sup> To test fitting procedure robustness, we propose a reliable and fully reproducible assessment protocol. The protocol is based on a synthetic dataset of optoelectronic characterizations generated by a two-dimensional (2D) drift-diffusion model.<sup>26</sup> We apply it to two fitting procedures: the direct fitting of I-V characteristic alone and a more complex method that considers multiple characterizations.<sup>13</sup> To identify possible multiple local optima and discuss error bars, we work with Bayesian tools as in a previous contribution.<sup>19</sup>

We demonstrate that parameters extracted solely from the I-V curve are not reliable and we illustrate with a clear example the typical misinterpretation that may arise. Then, we show that many of the issues identified with this approach can be mitigated if one considers more than a single characterization technique.<sup>13</sup> After identifying and discussing some limitations of the procedure given in Ref. 13, we present an improved procedure that requires fewer optoelectronic characterizations for the fit and obtains better agreement to the data, even for characterizations not exploited for inference. As none of the evaluated procedures retrieve the values of the parameters chosen for the 2D model, the physical meaning of the effective parameters obtained is discussed.

## II. METHODOLOGY

### A. Robustness evaluation protocol

Proving that a fitting procedure is trust-worthy is difficult, because an independent validation of the parameters obtained is typically lacking. However, it is easy to confirm that this procedure performs adequately in a simulated context where the ground-truth (GT) is known.

In this work, the robustness of several parameter estimation procedures is evaluated according to a protocol depicted in Fig. 2: 1) ground-truth parameters  $\theta_{\text{ref}}$  are chosen to generate the reference data  $Y_{\text{ref}}$ , from a model  $\mathcal{M}_r$  considered at least as realistic as the model  $\mathcal{M}_i$  used for inference; 2) a parameter estimation procedure  $\mathcal{P}[\mathcal{M}_i]$  is applied to  $Y_{\text{ref}}$ ; and 3) the inferred parameters  $\theta_{\text{est}}$  are compared to  $\theta_{\text{ref}}$ . This validation is necessary but insufficient because the reference-generation model  $\mathcal{M}_r$  may fail to account for processes that influence real measurements.

The synthetic reference data  $Y_{\text{ref}}$  is generated using a realistic 2D model, denoted by  $\mathcal{M}_r$  in Fig. 2, already reported in another publication.<sup>26</sup> In contrast, the fitting procedures  $\mathcal{P}$  rely on a 1D effective medium model  $\mathcal{M}_i$ , as described for instance in Refs. 9 and 13. To simulate  $Y$  and  $Y_{\text{ref}}$ , both models were implemented in the finite elements software COMSOL Multiphysics<sup>®</sup>.<sup>30</sup>  $Y_{\text{ref}}$  is comprised of a set of up to eight synthetic measurements, using six characterization techniques, summarized in Table I. To account for the measurement noise, a perturbation is added to  $Y_{\text{ref}}$ , drawn from a normal distribution with zero-mean and a standard-deviation  $\sigma_{\text{ref}}$  taken from datasheet specifications of each apparatus.<sup>27–29</sup>

### B. Bayesian inference

In least-square fitting procedures, the root mean square error (RMSE) quantifies the disagreement between a reference dataset  $Y_{\text{ref}}$  and the prediction  $Y(\theta)$  of a fitting model  $\mathcal{M}_i$ . It is to be minimized with respect

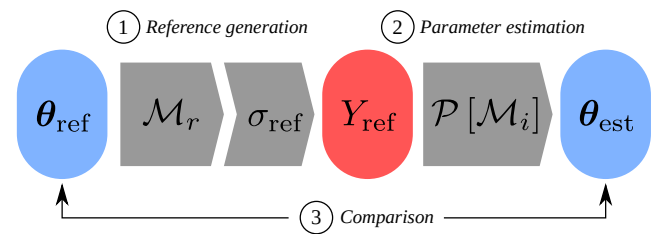


Figure 2. Evaluation protocol for parameter estimation procedure  $\mathcal{P}[\mathcal{M}_i]$ . Inferred parameters  $\theta_{\text{est}}$  are compared to the ground-truth  $\theta_{\text{ref}}$  taken to generate synthetic data  $Y_{\text{ref}}$  from model  $\mathcal{M}_r$  and apparatus noise  $\sigma_{\text{ref}}$ .

Table I. Characterization data included in the reference datasets. For this work we follow the definitions from Ref. 13.

Abbreviation	Measurement	Conditions	Apparatus	Ref.
dark I-V	I-V curve	In the dark.	Keithley 2420	27
light I-V	I-V curve	Under 1 sun illumination.	Keithley 2420	27
dark-CELIV	CELIV	In the dark.	R&S RTM3004	28
photo-CELIV	CELIV	After exposure to 1 sun illumination.	R&S RTM3004	28
TPC	Transient Photo-Current	Switch from 0 to 1 sun illumination at short-circuit.	R&S RTM3004	28
C-freq	Capacitance-frequency	AC perturbation around short-circuit conditions.	Agilent 4294A	29
dark C-V	Capacitance-voltage	AC perturbation around each point of the dark I-V curve.	Agilent 4294A	29
TPV	Transient Photo-Voltage	Switch from 1 to 0 sun illumination at open-circuit.	R&S RTM3004	28

to the model's parameters  $\theta$ , and is defined as

$$\text{RMSE}(\theta) = \sqrt{\frac{1}{m} \sum_{j=1}^m w_j (Y_j(\theta) - Y_{\text{ref},j})^2} \quad (1)$$

where  $Y_{\text{ref}} = \{Y_{\text{ref},j}, j \in 1, \dots, m\}$  are  $m$  reference datapoints,  $Y(\theta) = \{Y_j, j \in 1, \dots, m\}$  is the corresponding prediction of  $\mathcal{M}_i$ , and  $w = \{w_j, j \in 1, \dots, m\}$  are weighting factors.

Least-square fitting can be seen as a special case of the Bayesian approach to parameter estimation. Instead of the RMSE, the Bayesian picture considers the posterior probability density  $p(\theta | Y_{\text{ref}})$ , the probability density of  $\theta_{\text{ref}}$  being equal to  $\theta$ , posterior to the experimental observation  $Y_{\text{ref}}$ . It is given by<sup>31</sup>

$$p(\theta | Y_{\text{ref}}) \propto p(Y_{\text{ref}} | \theta) \times p(\theta) \quad (2)$$

where  $p(Y_{\text{ref}} | \theta)$  is the likelihood of observing  $Y_{\text{ref}}$ , if the hypothesis  $\theta = \theta_{\text{ref}}$  is true, and  $p(\theta)$  is the density of probability of  $\theta_{\text{ref}}$  being equal to  $\theta$ , prior to the observation. The likelihood is often expressed as the product of independent probabilities of observing each datapoint  $Y_{\text{ref},j}$ <sup>19</sup>

$$p(Y_{\text{ref}} | \theta) \propto \prod_{j=1}^m \exp \left[ -\frac{1}{2} \left( \frac{Y_j(\theta) - Y_{\text{ref},j}}{\sigma_j} \right)^2 \right] \quad (3)$$

where  $\sigma_j$  quantifies the measurement uncertainty.

From Eqs. (1)–(3), the relation between these two points of view may be highlighted by considering the logarithm of the posterior probability density

$$\log(p(\theta | Y_{\text{ref}})) = \frac{-m \cdot \text{RMSE}(\theta)^2}{2} + \log(p(\theta)) + C \quad (4)$$

where the RMSE weights are chosen as  $w_j = 1/\sigma_j^2$ , and  $C$  is a normalization constant independent of  $\theta$ .

The prior distribution  $p(\theta)$  expresses the knowledge already available before the observation of  $Y_{\text{ref}}$ . Such knowledge may originate from physical constraints or previous measurements, and generally lacks a sharp peak, reflecting one's ignorance about the true value of  $\theta$ . In contrast, the posterior distribution  $p(\theta | Y_{\text{ref}})$  ideally features one or several modes for parameter choices that

best explain  $Y_{\text{ref}}$ . Under these conditions, it is apparent from Eq. (4) that minimizing the RMSE can be interpreted as a maximization of the posterior probability. In both cases, extremization leads to the most probable value of  $\theta$ , given the observation  $Y_{\text{ref}}$  and inference model  $\mathcal{M}_i$ .

In addition, the probabilistic Bayesian picture stresses the relevance of computing a *credible region* in which the true  $\theta$  lies with a high probability, rather than a single best value. On the practical side this shifts the focus away from local minimization to global sampling, which can be achieved by state-of-the-art Markov Chain Monte Carlo (MCMC) algorithms.<sup>32,33</sup>

Because the Bayesian picture offers a more comprehensive view of the parameter space, this work leverages MCMC sampling for parameter estimation. This is achieved with a custom implementation of the *emcee* Python library.<sup>33</sup> A full description of its well-established algorithm can be found in Refs. 32 and 33. Its main features are outlined here to help the discussion. To sample the posterior distribution  $p(\theta | Y_{\text{ref}})$ , a set of walkers iteratively explores the parameter space, in parallel. At each iteration, walker positions are updated by using the stretch-move rule, a Markovian process.<sup>33</sup> During an initial *burn-in phase*, the walkers discover the search-space while being statistically pulled towards the posterior modes. In the stationary regime, or *sampling phase*, the walker positions obtained at every new iteration are independent samples drawn from the posterior distribution. For all the MCMC sampling presented in this work, 64 walkers were used. From the resulting Markov chains, one can compute a *credible interval* for each parameter  $\theta_j$ . We report the 16th–84th percentile interval of the collected samples because it coincides with the  $\mu \pm \sigma$  interval when the posterior probability density is a normal distribution with mean  $\mu$  and variance  $\sigma^2$ . It contains the true value of the parameter with a 68% probability. Further information about the Bayesian picture of parameter estimation can be found in the dedicated literature.<sup>31,32</sup>

### C. Reference datasets and uncertainties

In order to demonstrate that the results discussed are independent of the GT choice, the analysis is repeated

Table II. Geometrical parameter settings used for the simulation of the reference datasets, as defined in Fig. 1c.

Ground truth, $\theta_{\text{ref},i}$	$L$ (nm)	$S$ (mm <sup>2</sup> )	$W_n$ (nm)	$W_p$ (nm)	$a$ (nm)	$N_{\text{per}}$
1 - Symmetric	100	10	20	20	10	4
2 - Asymmetric	85	4.5	10	10	0	–

with two different sets of parameters, hereafter referred to as  $\theta_{\text{ref},1}$  and  $\theta_{\text{ref},2}$ . The former is chosen such that the donor and acceptor materials are symmetric to one another (same physical properties). Moreover, the tortuous conduction pathways of the input geometry are identical for the donor and acceptor domains, as shown in Fig. 1b. This ideal situation is helpful to test the reliability of a parameter estimation procedure. If the effective parameters  $\theta_{\text{est}}$  are not symmetric, their interpretation will be misleading because it will place undue blame for poor performances on one moiety rather than the other. Tables II and III list the parameter values corresponding to  $\theta_{\text{ref},1}$ .

$\theta_{\text{ref},2}$  was chosen to be similar to the values found in Table 2 of Ref. 13, for which one of the evaluated procedures  $\mathcal{P}$  was initially presented. That procedure is therefore expected to perform well when applied to the corresponding reference dataset. Geometric parameters are chosen to emulate the so-called checkerboard geometry, featuring straight conduction pathways with no tortuosity. The parameter values used for this GT can be found in Tables II and VI. Note that it is asymmetric as it does not have identical moieties.

Tabulated GT values for  $G_{\text{eff}}$  are the spatial average of the free carriers generation rate in 2D simulations.

The uncertainty factors  $\sigma_j$  for each datapoint  $j$  are an important set of hyper-parameters. They represent how accurately the model is expected to reproduce the measurement. A natural lower bound for  $\sigma_j$  is  $\sigma_{\text{ref},j}$ , the uncertainty directly imputable to the measuring apparatus: any attempt to reproduce the measurement beyond that accuracy limit implies fitting the noise of the instrument. Additional disagreement between the reference and the prediction comes from the choice of an approximate 1D model, which cannot reproduce the finest details of the synthetic measurements. Failure to acknowledge this model error also leads to overfitting, and slows down MCMC convergence considerably.

In our experience, using  $\sigma_j = \sigma_{\text{ref},j}$  yields artificially small error bars on I-V curves and impedance measurements, and in practice it is not possible to fit the prediction to the data with that level of accuracy, suggesting that the discrepancy is dominated by model error. Moreover, the noise level from the Keithley 2420 SMU is so much smaller than that of the Agilent 4294A analyzer that the dark C-V measurement would be effectively ignored by the procedure. For each apparatus, we therefore apply a weighting factor  $\delta_a$  to  $\sigma_{\text{ref},j}$ . Empirically, we found that all measurements contribute comparable

terms to the RMSE by setting  $\delta_a = 40$  for the SMU;  $\delta_a = 4$  for the impedance analyzer; and  $\delta_a = 1$  for the oscilloscope.

The whole reference datasets 1 and 2, associated with  $\theta_{\text{ref},1}$  and  $\theta_{\text{ref},2}$ , are shown as black symbols in Figs. 4 and 6, respectively. The uncertainties  $\sigma_j = \delta_a \cdot \sigma_{\text{ref},j}$  used for inference are displayed as error bars in all frames, except for transient measurement frames where the  $Y_j \pm \sigma_j$  region is shaded in gray.

### III. RESULTS AND DISCUSSION

#### A. Parameter estimation from current-voltage characteristics alone

Considering solely the light I-V measurement taken from the reference dataset 1, the MCMC procedure is used to search for the values of the following parameters: the carrier mobilities ( $\mu_n$ ,  $\mu_p$ ), the effective free-carrier generation rate  $G_{\text{eff}}$ , the bimolecular recombination rate  $k_{\text{rec}}$ , the built-in voltage  $V_{\text{bi}}$ , the extraction barriers ( $\varphi_{\text{cat}}$ ,  $\varphi_{\text{an}}$ ), and the parallel resistance  $R_p$ . The device thickness  $L$ , active area  $S$ , series resistance  $R_S$ , and relative permittivity  $\epsilon_r$  are assumed to be known accurately and kept equal to their GT value during the extraction. The starting points of the procedure are randomly drawn within a broad region of realistic values centered around  $\theta_{\text{ref},1}$ . The parameters  $\mu_n$ ,  $\mu_p$ ,  $R_p$ , and  $k_{\text{rec}}$  are mapped to a logarithmic scale (log-scale) to accelerate MCMC convergence.

Three local minimum of I-V curve's RMSE (i.e. modes) are detected after 1000 iterations. Sampling such a multimodal distribution can be slow using *emcee*. Therefore, credible intervals were obtained by sampling each mode separately for an additional 1000 iterations. The results are summarized in Table III.

Table III. Ground-truth and inferred parameters for reference dataset 1 solely using light I-V curve for the fit. Error bars denote the credible interval obtained by MCMC sampling.

Parameter	Unit	Ground truth	Mode 1 <sup>a</sup>	Mode 3
$R_p$	M $\Omega$	160.0	$17^{+673}_{-16}$	$226^{+1482}_{-198}$
$G_{\text{eff}} \times 10^{-21}$	1/(cm <sup>3</sup> s)	1.199	$1.184^{+0.007}_{-0.011}$	$1.172^{+0.004}_{-0.005}$
$\sqrt{\mu_n \times \mu_p} \times 10^8$	m <sup>2</sup> /(V s)	1.0	$3.5^{+3}_{-0.9}$	$0.27 \pm 0.01$
$\sqrt{\mu_n / \mu_p}$	1	1.0	$2.0^{+1.7}_{-0.4}$	$1.00^{+0.03}_{-0.04}$
$\varphi_{\text{cat}}$	mV	200	$365^{+30}_{-16}$	$60^{+53}_{-41}$
$\varphi_{\text{an}}$	mV	200	$101^{+71}_{-66}$	$70^{+56}_{-49}$
$V_{\text{bi}}$	V	1.0	$1.07 \pm 0.07$	$1.28^{+0.06}_{-0.07}$
$k_{\text{rec}} \times 10^{16}$	m <sup>3</sup> /s	1.206	$3.9^{+10.2}_{-1.8}$	$0.029 \pm 0.003$
RMSE	1		$19.2^{+1.0}_{-2.7}$	$1064.1^{+0.9}_{-2.1}$

<sup>a</sup> Modes 1 and 2 are symmetric: mode 2 is deduced from mode 1 by exchanging donor and acceptor roles.



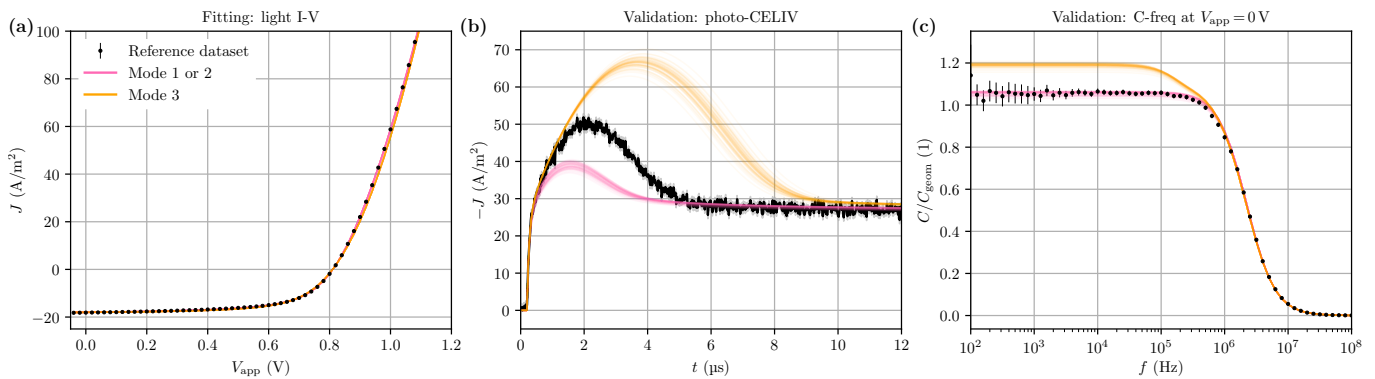


Figure 3. Parameter extraction from light I-V curves alone may fail to generalize to other measurements. Reference dataset 1 is shown with error bars (black symbols), along with predictions  $Y(\theta_{\text{est}})$  from I-V curve regression as a bundle of 64 curves. a) light I-V curve (fitting); b) photo-CELIV transient (cross-validation); and c) C-freq response at  $f = 1$  kHz (cross-validation).

As  $\mu_n$  and  $\mu_p$  show strong correlations, the variables  $\sqrt{\mu_n \times \mu_p}$  and  $\sqrt{\mu_n / \mu_p}$  are considered instead. In log-scale, they relate to the original variables through an affine transformation, hence *emcee* sampling is not affected by this change.<sup>33</sup> Modes 1 and 2 are broad and feature imbalanced physical properties, but are symmetric to each other. Therefore, the parameters of mode 2 are deduced from mode 1 by swapping the roles of the two moieties (donor and acceptor). Due to the same intrinsic symmetry of  $\mathcal{M}_i$ , modes 1 and 2 give exactly the same response  $Y(\theta)$ . Hence, mode 2 is not discussed further. In contrast, mode 3 features balanced mobilities, though an order magnitude smaller, and a recombination rate 34 times smaller than Langevin theory.

Fig. 3a shows that the I-V characteristics at the last MCMC iteration for modes 1 (pink bundle of curves) and 3 (orange bundle) agree visually with the characterization data exploited for fitting (black symbols). In spite of this apparent success, it is clear from Table III that the inferred parameters are not reliable: estimates from mode 1 and 2 are so broad that the error bars allow for only one significant figure on mobilities, recombination rate or parallel resistance. Besides, the lowest RMSE is observed for mode 1, which features imbalanced carrier mobilities and extraction barriers. Interpretation of the device’s performance in terms of these effective parameters is therefore misleading, as one may incorrectly conclude that the next best experimental step is to focus on hole transport, wasting time and resources. It is clear in this numerical experiment that neither moiety intrinsically performs worse than the other. Mode 3 captures the symmetry of the GT parameters, but its RMSE is two orders of magnitude larger than mode 1.

To discriminate the modes, the parameters can be validated against other characterizations of the reference. The final walkers positions are taken as input parameters to generate responses for each control measurement listed in Table I. Since it has a very small computational cost, this validation is advisable whenever the characterization data is available. Results are shown on Fig. 3b and

Fig. 3c for photo-CELIV and C-freq curves, respectively. Clearly, none of these modes manage to appropriately fit all measurements at once. Another approach is therefore necessary to yield the physical parameters.

## B. Parameter estimation from multiple characterizations

A natural remedy to the concerns raised in Sec. III A would be to work with 2D or 3D models for inference tasks to benefit from an explicit morphology description. Although this solution has been employed successfully in the past, the increase in computation times is so large that it is too time-consuming in many practical cases.<sup>19</sup>

As an alternative, several authors have suggested using more than one measurement to constrain the fit and avoid misleading interpretations based on I-V curves alone.<sup>12,13</sup> Neukom *et al.* have recently illustrated the use of a broad set of measurements for this task.<sup>13</sup> They outlined a seven-step estimation procedure by associating parameters to the measurement from which they are most easily deduced, as stated in Table IV. The first six steps, from A to F, provide the first estimate of  $\theta$ , which then serves as a starting point to the global fitting step G.

In this section, the robustness of this procedure is evaluated. In addition, we discuss important settings that are

Table IV. Summary of the parameter extraction steps of the procedure proposed in Ref. 13.

Step	Characterization data	Extracted parameters
A	dark-CELIV	$\varepsilon_r$
	C-freq	$R_S$
B	dark I-V	$R_p$
C	light I-V	$G_{\text{eff}}$
D	TPC	$\mu_n, \mu_p$
E	light I-V, dark C-V	$\varphi_{\text{cat}}, V_{\text{bi}}, \varphi_{\text{an}}$
F	photo-CELIV	$\gamma$
G	all of the above	$\mu_n, \mu_p, \varphi_{\text{cat}}, V_{\text{bi}}, \varphi_{\text{an}}, \gamma$

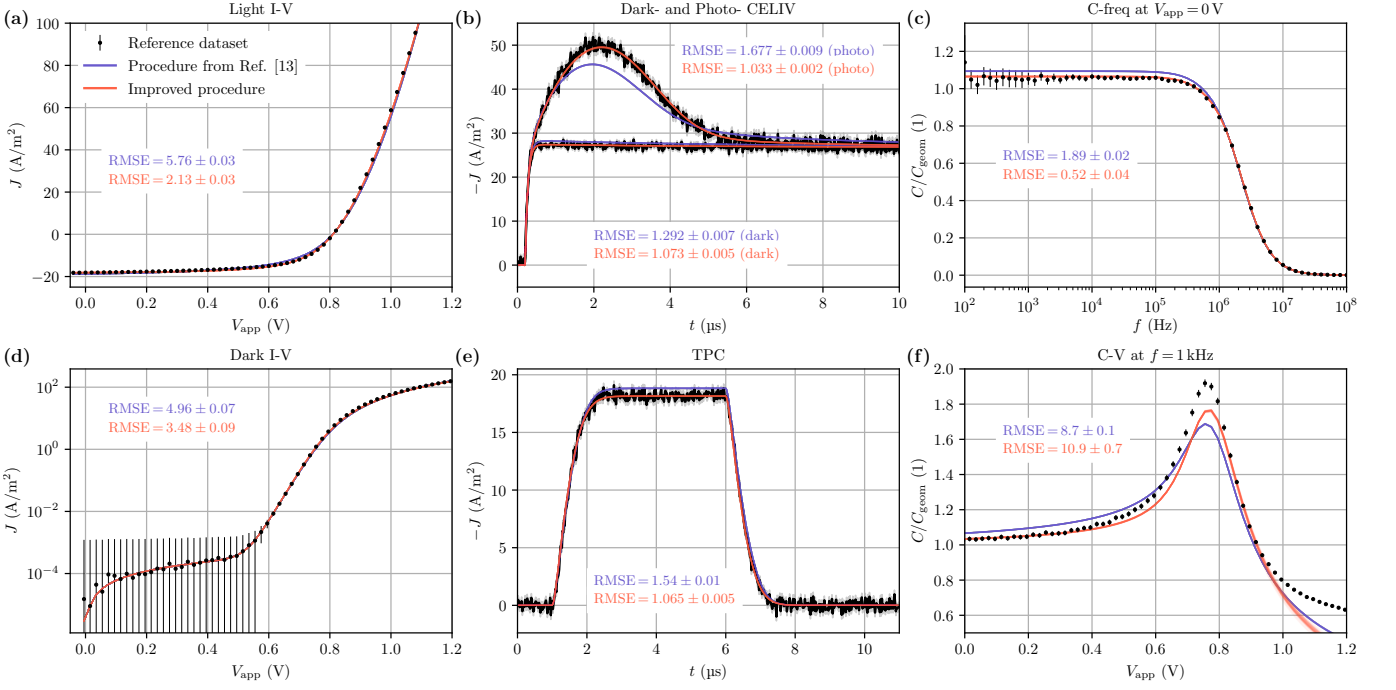


Figure 4. Reference dataset 1 (black symbols), along with predictions from the procedure taken from Ref. 13 (blue curves) and our proposed procedure (red curves). Fitting results are shown as a bundle of 64 predictions  $Y(\theta_{\text{est}})$ , obtained from the last MCMC iteration. Bundle spread illustrates the uncertainty on  $\theta_{\text{est}}$ , propagated to  $Y(\theta_{\text{est}})$ . The uncertainties  $\sigma_j = \delta_a \cdot \sigma_{\text{ref},j}$  used for inference are displayed as a gray region in frames (b) and (e) and as error bars elsewhere. A RMSE of 1 indicates that the prediction error is of the order of  $\sigma_j$ .

not explicitly reported or justified in Ref. 13. As mentioned in Sec. II, the evaluation protocol is applied to the two reference datasets shown in Figs. 4 and 6. Steps A, B, C, and F use local fitting approaches, whereas steps D and E are performed over 200 MCMC iterations, and the global fitting step G is performed over 500 MCMC iterations.

## 1. Ground-truth 1

*a. Step A* The plateau current value  $I_\infty$  of the dark-CELIV measurement (Fig. 4b) is directly related to the geometric capacitance  $C_{\text{geom}}$ . If the aspect ratio  $S/L$  is known, the relative permittivity  $\varepsilon_r$  can be deduced from the relation:

$$I_\infty = \mathcal{A} \cdot C_{\text{geom}} = \mathcal{A} \cdot \varepsilon_0 \varepsilon_r \cdot S/L \quad (5)$$

where  $\mathcal{A}$  is the slope of the CELIV voltage ramp.

A slope  $\mathcal{A} = -100$  V/ms was applied during 30  $\mu\text{s}$ . The current is averaged over the 20 to 30  $\mu\text{s}$  interval, where it has reached saturation. At a sampling rate of 100 points/ $\mu\text{s}$ , this provides enough statistics to cancel the noise from the apparatus.

We obtain  $C_{\text{geom}} = 2.656 \pm 0.002$  nF from the data, and if  $L$  and  $S$  are known perfectly, this gives directly  $\varepsilon_r = 3.000 \pm 0.002$  which matches the GT. Otherwise, the uncertainties from  $L$  and  $S$  must be propagated to the

error bar of  $\varepsilon_r$ . Because a 1D model is used here, one should keep in mind that the value of  $\varepsilon_r$  extracted is only an effective value, averaged over the entire junction.

With  $C_{\text{geom}}$  known, the capacitance of the device in the high-frequency region (Fig. 4c) is then fitted to

$$C(\omega) = \frac{C_{\text{geom}}}{1 + (\omega/\omega_c)^2} \quad (6)$$

where the cutoff frequency  $\omega_c$  depends on  $R_S$  according to the expression

$$\omega_c = 1/(R_S \cdot C_{\text{geom}}). \quad (7)$$

Here, a series resistance of  $R_S = 20.1 \Omega$  is found, in good agreement with the GT value  $R_S = 20 \Omega$ .

*b. Step B* The Ohmic regime of the dark I-V curve (Fig. 4d) is fitted to estimate the parallel resistance  $R_p$ , yielding  $R_p = 167.3 \text{ M}\Omega$ , again in reasonable agreement with the GT.

*c. Step C* The effective free-carrier generation rate  $G_{\text{eff}}$  is adjusted to reproduce the short-circuit current  $J_{\text{SC}}$  at one sun (Fig. 4a). A simple bisection algorithm is efficient here because only one parameter is extracted, and  $G_{\text{eff}}$  is bounded by the incoming photon flux  $G_{\text{opt}}$ . Ten iterations are sufficient to reach a precision of 0.1% of  $G_{\text{opt}}$ , yielding  $G_{\text{eff}} = 1.267 \times 10^{21}$  1/(cm<sup>3</sup>s), a moderate 6% overestimation from the GT.

*d. Step D* The electron and hole mobilities are extracted from the normalized TPC measurements (Fig. 4e). In order to construct a complete picture of the parameter space, we sample it with our MCMC procedure. Here again,  $\mu_n$  and  $\mu_p$  are set to vary in log-scale because this produces much faster convergence in our experience.

Fig. 5a shows the RMSE landscape as a function of  $(\mu_n, \mu_p)$ , obtained by interpolating over a broad sampling of the plane. Three local minima are indicated with red crosses, while the black reticle indicates the GT values used to generate the reference data. After the Markov chains have stabilized, a dominant mode with balanced mobility is found for  $\mu_n = (8.2 \pm 0.3) \times 10^{-8} \text{ m}^2/(\text{V s})$  and  $\mu_p = (8.1 \pm 0.3) \times 10^{-8} \text{ m}^2/(\text{V s})$  (A-label in Fig. 5). It is also the global RMSE minimum. The extracted mobilities underestimate the GT by about 20% but, more importantly, the symmetry issues raised in Sec. III A no longer correspond to the dominant modes.

Normalizing TPC implies that the dependence of  $J_{\text{SC}}$  on carriers mobility will not affect the fitting agreement. In principle, this allows step D to focus on the time-dependence of the current rise and decay. However it may yield surprising results when using a local minimization procedure such as Levenberg-Marquardt.<sup>34–36</sup> Indeed, in

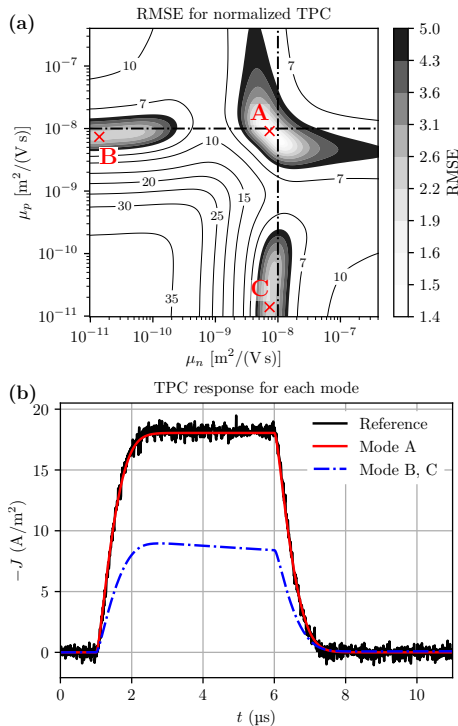


Figure 5. a)  $\text{RMSE}(\theta)$  landscape at step D when TPC response is normalized. Local minima are denoted by letter-labeled red crosses. The black dash-dotted reticle indicates the position of the ground-truth; b) Corresponding TPC response for each local minimum. Notice that minima B and C are superimposed because swapping moieties does not affect output currents.

addition to the dominant (balanced) mode A, Fig. 5a reveals the presence of two spurious modes (red crosses labeled B and C) with imbalanced mobilities, separated by almost three decades. If a local fitting procedure is initialized in the proximity of these two modes, the extracted mobilities may be biased.

Although the RMSE has a clear attraction sink for all three modes if the transient currents are normalized, the current density of the TPC plateau is underestimated by the two spurious modes by more than a factor of two, as shown on Fig. 5b. Clearly, they can only exist if one chooses to normalize the currents, which seems counter-productive.

*e. Step E* For this step, the built-in voltage  $V_{\text{bi}}$ , along with extraction barriers  $\varphi_{\text{cat}}$  and  $\varphi_{\text{an}}$ , is extracted from I-V and C-V characteristics. In their article,<sup>13</sup> Neukom *et al.* stressed the importance of I-V curve's first quadrant ( $V > 0, J > 0$ ), as it may reveal the presence of extraction barriers. Therefore, we ramp the voltage from 0 to 1.5 V, roughly twice the reference's open-circuit voltage ( $V_{\text{OC}}$ ), as shown on Figs. 4a and 4f.

During this step, only the  $V_{\text{OC}}$  and the C-V peak position ( $V_{\text{peak}}$ ) are adjusted. We noticed that they both vary linearly with the sum  $V_{\text{gap}} \equiv V_{\text{bi}} + \varphi_{\text{cat}} + \varphi_{\text{an}}$  in the range of parameter values visited by MCMC. Therefore, the procedure uses the additional degrees of freedom (two out of three) to attempt to recover fine details of the I-V and C-V curve's injection regimes, which are subject to a strong model error. As a result, the barrier values obtained at this stage appear to be arbitrary, and it is more meaningful to extract the value of  $V_{\text{gap}}$ . We obtain  $V_{\text{gap}} = 1.4934 \pm 0.0001 \text{ V}$ , a +7% deviation from the GT. The error bar is two orders of magnitude smaller than  $k_B T/q \simeq 26 \text{ mV}$ , the smallest voltage appearing in the model. This reveals how sensitive the RMSE is to  $V_{\text{gap}}$ , a consequence of the magnitude of the SMU uncertainty around  $V_{\text{OC}}$  ( $\sim 0.1 \mu\text{A}$ ).

*f. Step F* For this step, the recombination prefactor  $\gamma$  is varied in order to match the photo-CELIV measurements (Fig. 4b). Because there is only one degree of freedom, it is sufficient to perform a brute-force search by varying  $\gamma$  logarithmically from  $10^{-2}$  to  $10^{+2}$ . Within this range, the RMSE exhibits a clear minimum at  $\gamma = 0.293$ , about three times lower than Langevin recombination ( $\gamma = 1$ ).

*g. Step G* For this step, a global fitting procedure is run using MCMC sampling. As shown by the blue bundle of curves in Fig. 4, a relatively good agreement is obtained for nearly all measurements involved in the fitting procedure. However, the low-frequency capacitance or the C-V peak magnitudes are not reproduced within the error bars. Likewise, while the time-scales involved in the CELIV measurements are correctly reproduced, the height of the photo-CELIV peak is underestimated by the model. Finally, the decrease in capacitance in the injection regime ( $V > V_{\text{peak}}$ ) is found to be consistently steeper in the 1D model than the 2D reference. These discrepancies result from the 1D model being unadapted

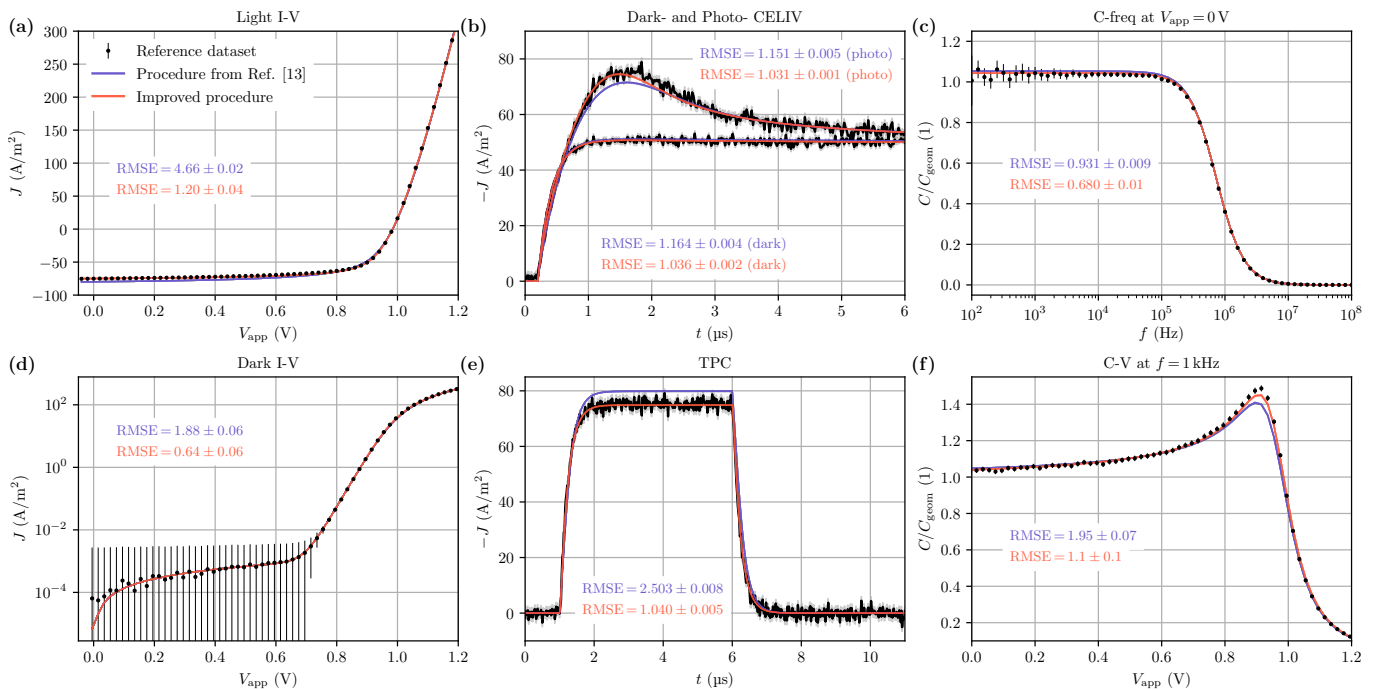


Figure 6. Reference dataset 2 (black symbols), along with predictions from the procedure taken from Ref. 13 (blue curves) and our proposed procedure (red curves). Fitting results are shown as a bundle of 64 predictions  $Y(\theta_{\text{est}})$ , obtained from the last MCMC iteration. Bundle spread illustrates the uncertainty on  $\theta_{\text{est}}$ , propagated to  $Y(\theta_{\text{est}})$ . The uncertainties  $\sigma_j = \delta_a \cdot \sigma_{\text{ref},j}$  used for inference are displayed as a gray region in frames (b) and (e) and as error bars elsewhere. A RMSE of 1 indicates that the prediction error is of the order of  $\sigma_j$ .

to describe the reference. As a result, the fitting step is forced to accept contradictory compromises between different measurements.

Despite the uneven agreement, one can notice from Table V that the estimations of the energy levels have drastically improved with respect to step E. The new estimate  $V_{\text{gap}} = 1.4702 \pm 0.0002$  V is slightly closer to the GT (+5%). Finally, the mobilities have remained balanced but are now underestimated by as much as 30%. The full list of extracted parameters can be found in Table V.

*h. Cross-validation* In Ref. 13, the inferred parameters are cross-validated by showing that the model's predictions are in excellent agreement with TPV measurements, although not exploited for fitting. However, we find that a good agreement on TPV is reached already at step D, well before the procedure's end, while the parameters are still evolving significantly. This suggests that the TPV response is much easier to reproduce than other measurements, such as C-V or CELIV. In our experience, a set of parameters providing a satisfactory agreement at step G will always have a RMSE close to 1 on TPV, whereas the opposite is clearly not true. Therefore, the success of this cross-validation step should not significantly improve the credibility of the inferred parameters.

## 2. Ground-truth 2

It will now be shown that our main conclusions are not tied to a specific choice of GT, as they remain valid for  $\theta_{\text{ref},2}$  and the reference dataset 2.

*a. Steps A to C* Up to step C, no additional observation is to be made. The results from these steps are summarized in Table VI and confirm the precision and accuracy of the estimations obtained with the reference dataset 1.

*b. Step D* As can be noted from Table VI, the average mobility  $\sqrt{\mu_n \times \mu_p}$  of the GT is accurately reproduced, even though the error bars on estimates are much larger for this reference. The estimations of  $\mu_n$  and  $\mu_p$  are balanced, in spite of the mobility ratio  $\mu_n/\mu_p = 2$  associated with the GT. As for the reference 1, the time-scales of the TPC are well reproduced (Fig. 6e).

*c. Step E* This step confirms that the RMSE is solely controlled by  $V_{\text{gap}}$ . The Markov chains yield the value  $V_{\text{gap}} = 1.68417 \pm 0.00006$  V, which is again excessively precise, while it overestimates the GT by ca. 7%. The positions of  $V_{\text{OC}}$  and  $V_{\text{peak}}$  are correctly reproduced, but  $\varphi_{\text{cat}}$  and  $\varphi_{\text{an}}$  are estimated with only one significant figure since this stage fails to constrain the barriers.

*d. Step F* Again, step F is performed using a brute force search, in which  $\gamma$  varies logarithmically from  $10^{-2}$  to  $10^{+2}$ , minimizing the RMSE at  $\gamma = 0.215$ .



Table V. Ground-truth 1 and inferred parameters from the reference dataset 1. Parameter kept fixed to their partial fitting estimation are indicated by dashes. The error bars correspond to the 16th–84th percentile interval of the Markov chains. When  $p(\theta | Y_{\text{ref}})$  [Eq. (2)] is the normal distribution,  $\theta \sim \mathcal{N}(\mu, \sigma^2)$ ,  $\theta = \mu_{-m}^{+p}$  means that  $[\mu - m : \mu + p]$  is the  $\mu \pm \sigma$  interval.

Parameter	Unit	Ground truth, $\theta_{\text{ref},1}$	$\theta_{\text{est}}$ , method from Ref. 13			$\theta_{\text{est}}$ , improved procedure (this work)		
			Partial fit	(step)	Global fit	Partial fit	(step)	Global fit
$\varepsilon_r$		3	$3.000 \pm 0.002$	(A)	–	$3.000 \pm 0.002$	(A)	–
$R_S$	$\Omega$	20	20.1	(A)	–	20.1	(A)	–
$R_p$	$M\Omega$	160	167.3	(B)	–	167.3	(B)	–
$G_{\text{eff}} \times 10^{-21}$	$1/(\text{cm}^3\text{s})$	1.199	1.267	(C)	–	$1.275 \pm 0.001$	(D)	$1.160_{-0.002}^{+0.001}$
$\mu_n \times 10^8$	$\text{m}^2/(\text{V s})$	1.0	$0.82 \pm 0.03$	(D)	$0.71 \pm 0.01$	$0.80 \pm 0.02$	(D)	$0.79 \pm 0.01$
$\mu_p \times 10^8$	$\text{m}^2/(\text{V s})$	1.0	$0.81 \pm 0.03$	(D)	$0.71 \pm 0.01$	$0.79 \pm 0.02$	(D)	$1.04 \pm 0.01$
$\varphi_{\text{cat}}$	mV	200	$127_{-51}^{+12}$	(E)	$174_{-2}^{+1}$			$302 \pm 1$
$\varphi_{\text{an}}$	mV	200	$79 \pm 50$	(E)	$174 \pm 2$			$203 \pm 3$
$V_{\text{bi}}$	V	1.0	$1.30_{-0.02}^{+0.03}$	(E)	$1.123_{-0.001}^{+0.002}$			$0.956 \pm 0.003$
$V_{\text{gap}}$	V	1.4	$1.4934 \pm 0.0001$	(E)	$1.4702 \pm 0.0002$			$1.4598 \pm 0.0001$
$\gamma$		1.0	0.293	(F)	$0.466_{-0.003}^{+0.002}$			$0.213 \pm 0.002$

*e. Step G* Fig. 6 shows that the prediction of the last iteration of the global fitting step G (blue bundle) accurately reproduces the broad set of reference measurements (black symbols).

Impedance measurements (see Figs. 6c and 6f) are better reproduced for this reference dataset than for the previous one. In contrast, the short-circuit current (and therefore the TPC plateau) is overestimated, as visible on Figs. 6a and 6e, while the height of the photo-CELIV peak is underestimated. We attribute this to the fact that  $G_{\text{eff}}$  was fixed early in the procedure (see Table IV). Because  $J_{\text{SC}}$  has a strong impact on the overall RMSE, this likely hinders the procedure’s progress on other parameters as well.

The full list of extracted parameters can be found in Table VI. In particular, the estimate of  $V_{\text{gap}}$  improves (4% overestimation), but the individual barriers  $\varphi_{\text{cat}}$  and  $\varphi_{\text{an}}$  are far from the GT. A mobility ratio as large as  $\mu_n/\mu_p = 50$  is found, which severely exaggerates the difference between electron and hole transport.

### C. Improved parameter estimation procedure

Based on the observations made so far, we now suggest changes to Neukom *et al.*’s procedure.<sup>13</sup> The proposed modifications seek to address major issues raised in the previous section. Compared to the steps summarized in Table IV, the main alteration is to discard steps E and F while releasing  $G_{\text{eff}}$  at steps C, D and G.

#### 1. Step-by-step description of the procedure

*a. Steps A to C* As steps A, B and C are already providing adequate results, they were left unchanged, resulting in the same fitting quality on  $\varepsilon_r$ ,  $R_S$  and  $R_p$ .

However, keeping  $G_{\text{eff}}$  fixed afterwards is somewhat arbitrary since  $J_{\text{SC}}$  is dependent on the mobilities and the recombination rate, which are only extracted at a later stage. Hence,  $G_{\text{eff}}$  is adjusted in subsequent steps. An alternative could be to extract  $G_{\text{eff}}$  from the saturation current at high reverse bias, which is less sensitive to mobilities and recombination rate than  $J_{\text{SC}}$ .

*b. Step D* The main effect of  $G_{\text{eff}}$  is to linearly rescale the entire TPC response, but it has a little-to-no influence on the rise and decay times. Releasing this additional parameter should thus be sufficient to reproduce the plateau current at steady-state. Therefore, the TPC is no longer normalized at this stage. Combined, we expect that these two alterations are effective at removing the spurious modes of Fig. 5.

*c. Steps E and F* We found that extraction barriers estimated from step E are not reliable, and since  $V_{\text{gap}}$  is easy to recover during the global fit because it correlates linearly with  $V_{\text{OC}}$ , we suggest skipping this stage. One could expect step F to accelerate the convergence of the global fit as the estimation of  $\gamma$  is stable when moving from steps F to G. In practice, we found that this convergence boost was not significant, and we propose to ignore this step also.

*d. Step G* By monitoring the RMSE of each measurement from steps C to G, we noticed that some characterizations have a RMSE negligible compared to the total before they even participate in the fit. It suggests that they only contain information that is already captured by other measurements. For instance, the dark-CELIV is dominated by RC effects, also probed by the photo-CELIV. It makes dark-CELIV information redundant in an extraction stage where the photo-CELIV is already in use. Likewise, the dark I-V curve repeats information contained in the light I-V curve, except for the estimation of  $R_p$  at step B. Impedance measurements were not found to be redundant with any other technique, but in our experience, it is challenging to obtain a low RMSE

Table VI. Ground-truth 2 and inferred parameters from the reference dataset 2. Parameter kept fixed to their partial fitting estimation are indicated by dashes. The error bars correspond to the 16th–84th percentile interval of the Markov chains. When  $p(\theta | Y_{\text{ref}})$  [Eq. (2)] is the normal distribution,  $\theta \sim \mathcal{N}(\mu, \sigma^2)$ ,  $\theta = \mu_{-m}^{+p}$  means that  $[\mu - m : \mu + p]$  is the  $\mu \pm \sigma$  interval.

Parameter	Unit	Ground truth, $\theta_{\text{ref},2}$	$\theta_{\text{est}}$ , method from Ref. 13			$\theta_{\text{est}}$ , improved procedure (this work)		
			Partial fit	(step)	Global fit	Partial fit	(step)	Global fit
$\varepsilon_r$		4.7	$4.711 \pm 0.002$	(A)	–	$4.711 \pm 0.002$	(A)	–
$R_S$	$\Omega$	90	88.5	(A)	–	88.5	(A)	–
$R_p$	$M\Omega$	160	163.1	(B)	–	163.1	(B)	–
$G_{\text{eff}} \times 10^{-21}$	$1/(\text{cm}^3\text{s})$	5.922	6.230	(C)	–	$6.11^{+0.05}_{-0.02}$	(D)	$5.614 \pm 0.006$
$\mu_n \times 10^7$	$\text{m}^2/(\text{V s})$	1.6	$1.2^{+1}_{-0.4}$	(D)	$8.2^{+0.7}_{-0.5}$	$1.8 \pm 0.6$	(D)	$1.87^{+0.09}_{-0.10}$
$\mu_p \times 10^7$	$\text{m}^2/(\text{V s})$	0.8	$1.2^{+0.9}_{-0.4}$	(D)	$0.163 \pm 0.002$	$0.9 \pm 0.1$	(D)	$0.47 \pm 0.02$
$\varphi_{\text{cat}}$	mV	80	$84^{+28}_{-47}$	(E)	$46^{+4}_{-3}$			$170 \pm 3$
$\varphi_{\text{an}}$	mV	150	$81^{+30}_{-49}$	(E)	$214 \pm 1$			$176 \pm 3$
$V_{\text{bi}}$	V	1.34	$1.53^{+0.02}_{-0.02}$	(E)	$1.380^{+0.003}_{-0.004}$			$1.292^{+0.002}_{-0.003}$
$V_{\text{gap}}$	V	1.57	$1.68417 \pm 0.00006$	(E)	$1.6400^{+0.0005}_{-0.0002}$			$1.6371^{+0.0003}_{-0.0004}$
$\gamma$		1.0	0.215	(F)	$0.051^{+0.003}_{-0.004}$			$0.147 \pm 0.005$

on both transient and impedance measurements using the 1D model (see Sec. IIC).

As a result, we suggest using a reduced step G', in which only light I-V, TPC, and photo-CELIV measurements contribute to the RMSE. We expect these modifications to only have a minimal impact on the inference results while allowing faster convergence. Another approach, not explored in this work, would be to expand the effective 1D model in ways that allow to simultaneously reproduce impedance measurements and transient measurements equally well.

Restraining the number of fitting measurements in this way has three main advantages: 1) it reduces the fitting time by reducing the number of simulations run at each iteration; 2) convergence is expected to be reached in fewer iterations because contradictory requirements between transient and impedance responses are lifted; 3) the discarded measurements can either be spared (reducing the number of experiments required) or used to expand the cross-validation dataset.

Indeed, we argue that we achieve strong cross-validation of the inferred parameters by using  $\theta_{\text{est}}$  to predict the dark I-V, dark-CELIV, C-freq, dark C-V, and TPV curves. Among these five measurements, the C-freq and dark C-V curves are the most informative because they are not redundant with any other characterization. A small RMSE for these measurements is therefore indicative of a good fit, but it may not always be possible to achieve with a 1D model. At least,  $V_{\text{peak}}$  should be predicted as accurately as  $V_{\text{OC}}$ . In contrast, the dark I-V, dark-CELIV, and TPV curves are easier to reproduce. A large RMSE for these measurements would therefore suggest overfitting, but a small RMSE would be inconclusive.

During our reduced step G', the TPC characteristic is left without normalization, and  $G_{\text{eff}}$  is still released as a fitting parameter. Parameters  $\mu_n$ ,  $\mu_p$ , and  $\gamma$  are again

varied logarithmically because this reduces the number of iterations required for convergence.

## 2. Ground-truth 1

The proposed procedure is applied to the reference dataset 1. As stated above, and shown in Table V, the values for  $\varepsilon_r$ ,  $R_S$ , and  $R_p$  are unchanged compared to the previous procedure.

After convergence has been reached for step D, the mobilities are underestimated by about 20%, with balanced electron/hole transport. While  $G_{\text{eff}}$  increases by less than 1% compared to step C, the two spurious modes which failed to describe the TPC plateau have disappeared.

The predictions  $Y(\theta)$  obtained at the last MCMC iteration for step G' are displayed with red bundles of curves in Fig. 4. As can be noted, the agreement with the reference 1 is satisfactory across all measurements except the dark C-V curve (Fig. 4f).

Among the common dataset used by both procedures, it can be noted that the peak of the photo-CELIV is reproduced more accurately using our approach (Fig. 4b). We believe that this improvement was enabled by lifting the strong constraint of fitting transient and impedance measurements simultaneously. The RMSE of the light I-V (Fig. 4a), photo-CELIV (Fig. 4b), and TPC (Fig. 4e) curves are all smaller than those from Neukom *et al.*'s procedure.

Even though they were not part of the fitting dataset, the dark I-V (Fig. 4d), dark-CELIV (Fig. 4b), and C-freq (Fig. 4c) characteristics are all well reproduced. Moreover, their RMSE is reduced compared to Sec. III B. On the other hand, the dark C-V prediction still exhibits a marked deviation in the injection regime (Fig. 4f). This deviation is similar to the one already described in Sec. III B, but it is more pronounced, which leads to a

larger RMSE for that measurement overall.

$G_{\text{eff}}$  slightly improves during step G', with respect to step D. The average mobility was underestimated by about 10%, closer to the GT than the method from Ref. 13 (30%), whilst slightly unbalanced ( $\mu_p/\mu_n \simeq 1.32$ ). As can be noted from Table V, the inferred values of  $\varphi_{\text{cat}}$  and  $\varphi_{\text{an}}$  are strongly asymmetric, in spite of the symmetry of the GT. This corroborates the observation that  $\varphi_{\text{an}}$  and  $\varphi_{\text{cat}}$  are not independent parameters, but that the model is mainly sensitive to the aggregate parameter  $V_{\text{gap}} = \varphi_{\text{cat}} + V_{\text{bi}} + \varphi_{\text{an}}$ . While we find  $\varphi_{\text{an}} = 203 \pm 3 \text{ mV}$  in close agreement to the GT, this appears to be coincidental, as it has no reason to be better reproduced than  $\varphi_{\text{cat}}$ , for which we find a 100 mV deviation from the GT. However, if the analysis is limited to  $V_{\text{gap}}$  for which the extraction is the most sensitive,  $V_{\text{gap}} = 1.4598 \pm 0.0001 \text{ V}$ , which overestimates the true value of  $V_{\text{gap}}$  by only 4%. Provided that  $\varphi_{\text{an}}$  and  $\varphi_{\text{cat}}$  are measured independently, the fitting procedure presented here can therefore accurately extract the value of  $V_{\text{bi}}$ . The effective recombination rate is found to be reduced by a factor of 5 compared to Langevin theory. The full list of extracted parameters can be found in Table V.

### 3. Ground-truth 2

Fig 6 shows, with a red bundle of curves, the results of fitting the reference dataset 2 with our improved procedure, while extracted parameters are gathered in Table VI. Again, the parameter values obtained at steps A to C are the same as Neukom *et al.*'s approach.

As already discussed, swapping moieties in the model  $\mathcal{M}_i$  has no effect on output currents. Hence the posterior distribution obtained at step D must feature pairs of modes for the mobilities (possibly degenerated). Indeed, when a mode is found at  $(\mu_n, \mu_p) = (\mu_1, \mu_2)$ , then another is to be found at  $(\mu_n, \mu_p) = (\mu_2, \mu_1)$ . Without loss of generality, it is enough to consider the case  $\mu_n > \mu_p$ , as before, and to perform inferences on  $\mu_n = \max(\mu_1, \mu_2)$  and  $\mu_p = \min(\mu_1, \mu_2)$ .

Here,  $\mu_n$  and  $\mu_p$  are correlated with  $G_{\text{eff}}$ , even if the latter only varies within a  $\pm 3\%$  range. In that context, it is not appropriate to define consistent credible regions for  $G_{\text{eff}}$ ,  $\mu_n$ , and  $\mu_p$  by the direct read of the percentile intervals. It is important to realize that due to correlations, independent values of  $G_{\text{eff}}$ ,  $\mu_n$  and  $\mu_p$  cannot be extracted. At this stage (step D), this is not an issue because the final MCMC walkers' positions can be used as the starting positions of the next stage. Indeed, contrarily to a local minimization procedure, MCMC approaches are able to represent the parameter joint distributions in their complexity. The parameter correlation will be easier to reduce at step G', when a larger set of measurements is considered.

Nevertheless, it may be valuable to get an approximate sense of the location and spread of each parameter distribution. Therefore, we first consider a credible re-

gion  $\mathcal{C}$  for  $G_{\text{eff}}$  (16th–84th percentile interval), and then characterize the distributions of  $\mu_n$  and  $\mu_p$ , conditional on  $G_{\text{eff}} \in \mathcal{C}$  by fitting them to normal distributions. Using this scheme, we obtain values for  $G_{\text{eff}}$ ,  $\mu_n$  and  $\mu_p$  in close agreement with the GT, as reported in Table V. In particular we find a mobility ratio  $(\mu_n/\mu_p) = 2.1$ , in good agreement with the value of 2.0 of the GT. Of course, the error bars on mobilities are here conditional on the value of  $G_{\text{eff}}$  and thus underestimate the true uncertainties.

During step G', the mobility estimations lose some of their accuracy and the mobility ratio increases to 4. Because this ratio is large enough for the two mobility modes to be clearly separated, no special treatment is needed to analyze step G'. Therefore, all the procedures presented in this paper exaggerate mobility imbalance. The improved procedure does not solve this issue, but it reduces its magnitude by a decade compared to Sec. III B.

The accuracy on the estimation of  $V_{\text{gap}}$  is equivalent to Neukom *et al.*'s procedure (+4%). The full list of extracted parameters can be found in Table VI.

### D. Interpretation of the effective parameters

Previous sections have shown that considering distinct characterizations for fitting allows reaching a good agreement for most measurements. Nevertheless, it is apparent from Tables V and VI that the values of the ground-truth  $\theta_{\text{ref}}$  are generally not contained within MCMC error bars of the inferred parameters  $\theta_{\text{est}}$ . This demonstrates that the extracted parameters are only effective, and should be interpreted as such.

In particular, the effective generation rate  $G_{\text{eff}}$  is well reproduced by all procedures considered in this work, suggesting it can straightforwardly be interpreted as a volume averaged generation rate.

In contrast, the Langevin recombination rate prefactor  $\gamma$  is consistently observed to be lower than 1. As already pointed out by previous theoretical work, charge carriers are protected from recombination in the 2D model, because donor and acceptor domains are segregated whereas in the 1D effective medium model, bimolecular recombination occurs in the bulk of the active layer.<sup>5</sup> It is then expected that the effective  $\gamma$  of the 1D model must be lower than the GT to obtain the same overall recombination currents. Hence, caution is warranted when interpreting values of  $\gamma$  obtained from parameter estimations using 1D effective medium models.

Likewise, it has been proposed<sup>5,37</sup> that transit times of free carriers are affected by the details of the BHJ geometry. Apparent carrier mobilities are expected to be decreasing functions of the tortuosity. This could explain why the apparent mobilities obtained by fitting the TPC responses are 20% below the GT in the tortuous case ( $\theta_{\text{ref},1}$ ), but closer to the GT in the non-tortuous case ( $\theta_{\text{ref},2}$ ), as shown respectively in Tables V and VI. A clear rationale to predict the effective mobilities from the geometry is missing and would require

further research. While the effective parameters yielded by our procedure are not closer to the GT than Ref. 13, the global fitting step G' predicts the characterization datasets with higher accuracy.

Values of  $V_{\text{gap}}$  reported in Tables V and VI reveal that  $V_{\text{gap}}$  is overestimated by the procedures, even though  $V_{\text{OC}}$  and  $V_{\text{peak}}$  are well reproduced and the error bar on  $V_{\text{gap}}$  is smaller than the precision needed. This suggests that  $V_{\text{gap}}$  should also be considered as effective, which is consistent with the fact that the  $V_{\text{OC}}$  of BHJ devices is dependent on the morphology.<sup>38</sup>

Determining the meaning of these effective parameters is beyond the scope of this contribution, but crucial in order to avoid misleading conclusions from parameter extraction results.

#### IV. SUMMARY AND CONCLUSION

In this work, we have tested the robustness of three different fitting strategies for OPV characterization data. By generating synthetic but realistic device responses, we can express clear conclusions about each method's accuracy in a context that closely matches experimental conditions. As fitting procedures are ultimately about extracting parameters, this level of validation could not have been achieved using experimental measurements, for which ground-truth parameters are unknown.

We reiterate the literature's consensus that I-V data alone is insufficient to draw meaningful inferences about physical parameters, as defined in standard drift-diffusion models. In fact, following that approach is prone to misleading conclusions, wasting time and resources, as clearly demonstrated in Sec. III A.

Moreover, after having carefully evaluated the procedure proposed in Ref. 13 (see Sec. III B), we validated a modified procedure that leverages substantial improvements (see Sec. III C) to achieve a better accuracy with fewer measurements. In addition, using a global MCMC fitting procedure provides a better appreciation of the validity of the results, in the form of error bars, and the ability to detect several RMSE modes when they exist. While a MCMC fit typically requires more model evaluations than Levenberg-Marquardt, it can be run in parallel, on up to 32 processors in our case, and does not require evaluating the model's Jacobian. That makes our procedure suitable for high fidelity parameter extraction at the expense of higher computational cost. In this regard, replacing the MCMC sampling with a less model-intensive Bayesian sampler may enable lower computation times in the future without changing the overall structure of the procedure.

Regarding the extracted parameters obtained by the above-mentioned procedures, they are all associated to a 1D effective medium model as it needs less computational resources. While the obtained values did not match the ground-truth, these 1D effective parameters can adequately represent a broad set of device measure-

ments, especially in the non-tortuous case. Nonetheless, their values must be carefully interpreted as aggregated information from BHJ morphology and other physical properties.

Because a 1D model has fewer degrees of freedom than a 2D or 3D model, one can not hope to fully disentangle the exact physical parameters and the BHJ morphology from each other. The missing link, i.e., a detailed knowledge of the relationship between the morphology and the effective parameters, would be a significant step towards the understanding of structure-to-performance relationships in OPV cells.

#### ACKNOWLEDGMENTS

A.P. received financial support from the MSII French doctoral school (ED-269). The authors wish to thank Dr. M. Foesnau and Dr. Ch. Heinrich for fruitful discussions regarding Bayesian inference, Dr. D. Foreman-Mackey, Dr. J. Goodman and Dr. J. Weare for helpful discussion regarding the MCMC implementation applied in this work. Many thanks go to Dr. M. Neukom for his helpful feedback about our attempts to reproduce simulations from Ref. 13.

#### REFERENCES

- <sup>1</sup>EIA. International energy outlook. [Technical report, U.S. Energy Information Administration, 2019.](#)
- <sup>2</sup>T. Kober, H.-W. Schiffer, M. Densing, and E. Panos. Global energy perspectives to 2060—WEC's World Energy Scenarios 2019. *Energy Strategy Rev.*, **31**, 100523 (2020).
- <sup>3</sup>M. A. Green, E. D. Dunlop, J. Hohl-Ebinger, M. Yoshita, N. Kopidakis, and A. W.Y. Ho-Baillie. Solar cell efficiency tables (version 55). *Prog. Photovolt.*, **28**(1), 3–15 (2020).
- <sup>4</sup>I. Zonno, H. Zayani, M. Grzeslo, B. Krogmeier, and T. Kirchartz. Extracting Recombination Parameters from Impedance Measurements on Organic Solar Cells. *Phys. Rev. Appl.*, **11**(5), 054024 (2019).
- <sup>5</sup>T. Albes, P. Lugli, and A. Gagliardi. Investigation of the Blend Morphology in Bulk-Heterojunction Organic Solar Cells. *IEEE Trans. Nanotechnol.*, **15**(2), 281–288 (2016).
- <sup>6</sup>D. Bartsaghi, M. Turbiez, and L. J. A. Koster. Charge transport and recombination in PDPP5T:[70]PCBM organic solar cells: The influence of morphology. *Org. Electron.*, **15**(11), 3191–3202 (2014).
- <sup>7</sup>I. Hwang and N. C. Greenham. Modeling photocurrent transients in organic solar cells. *Nanotechnology*, **19**(42), 424012 (2008).
- <sup>8</sup>G. Richardson, C. P. Please, and V. Styles. Derivation and solution of effective medium equations for bulk heterojunction organic solar cells. *Eur. J. Appl. Math.*, **28**(06), 973–1014 (2017).
- <sup>9</sup>L. J. A. Koster, E. C. P. Smits, V. D. Mihailetschi, and P. W. M. Blom. Device model for the operation of polymer/fullerene bulk heterojunction solar cells. *Phys. Rev. B*, **72**(8), 085205 (2005).
- <sup>10</sup>L. J. A. Koster, V. D. Mihailetschi, and P. W. M. Blom. Bimolecular recombination in polymer/fullerene bulk heterojunction solar cells. *Appl. Phys. Lett.*, **88**(5), 052104 (2006).
- <sup>11</sup>Z. Tang, J. Wang, A. Melianas, Y. Wu, R. Kroon, W. Li, W. Ma, M. R. Andersson, Z. Ma, W. Cai, et al. Relating open-circuit voltage losses to the active layer morphology and contact selectivity



- in organic solar cells. *J. Mater. Chem. A*, **6**(26), 12574–12581 (2018).
- <sup>12</sup>Y. T. Set, T. Zhang, E. Birgersson, and J. Luther. What parameters can be reliably deduced from the current-voltage characteristics of an organic bulk-heterojunction solar cell? *J. Appl. Phys.*, **117**(8), 084503 (2015).
- <sup>13</sup>M. Neukom, S. Züfle, S. Jenatsch, and B. Ruhstaller. Optoelectronic characterization of third-generation solar cells. *Sci. Technol. Adv. Mater.*, **19**(PV1), 291–316 (2018).
- <sup>14</sup>H. Li and J.-L. Bredas. Modeling of actual-size organic electronic devices from efficient molecular-scale simulations. *Adv. Funct. Mater.*, **28**(29), 1801460 (2018).
- <sup>15</sup>J. J. M. van der Holst, M. A. Uijtewaal, B. Ramachandhran, R. Coehoorn, P. A. Bobbert, G. A. de Wijs, and R. A. de Groot. Modeling and analysis of the three-dimensional current density in sandwich-type single-carrier devices of disordered organic semiconductors. *Phys. Rev. B*, **79**(8), 085203 (2009).
- <sup>16</sup>A. G. Gagorik, J. W. Mohin, T. Kowalewski, and G. R. Hutchison. Monte Carlo Simulations of Charge Transport in 2D Organic Photovoltaics. *J. Phys. Chem. Lett.*, **4**(1), 36–42 (2013).
- <sup>17</sup>S. Wilken, T. Upreti, A. Melianas, S. Dahlström, G. Persson, E. Olsson, R. Österbacka, and M. Kemerink. Experimentally calibrated kinetic monte carlo model reproduces organic solar cell current-voltage curve. *Sol. RRL*, **4**(6), 202000029 (2020).
- <sup>18</sup>N. G. Martinelli, M. Savini, L. Muccioli, Y. Olivier, F. Castet, C. Zannoni, D. Beljonne, and J. Cornil. Modeling polymer dielectric/pentacene interfaces: on the role of electrostatic energy disorder on charge carrier mobility. *Adv. Funct. Mater.*, **19**(20), 3254–3261 (2009).
- <sup>19</sup>A. Raba, Y. Leroy, M. Kohlstädt, U. Würfel, and A. Cordan. Organic Solar Cells: Extraction of Physical Parameters by Means of Markov Chain Monte Carlo Techniques. *IEEE J. Photovolt.*, **7**(4), 1098–1104 (2017).
- <sup>20</sup>N. Majeed, M. Saladina, M. Krompiec, S. Greedy, C. Deibel, and R. C. I. MacKenzie. Using Deep Machine Learning to Understand the Physical Performance Bottlenecks in Novel Thin-Film Solar Cells. *Adv. Funct. Mater.*, **30**(7), 1907259 (2020).
- <sup>21</sup>A. R. Jordehi. Parameter Estimation of Solar Photovoltaic (PV) Cells: A Review. *Renew. Sust. Energy Rev.*, **61**, 354–371 (2016).
- <sup>22</sup>H. Liao, D. Qiao, C. Huang, and S. Li. Parameters Identification of Photovoltaic Cells Based on Differential Evolution Algorithm. *ITM web Conf. (Impr.)*, **7**, 04003 (2016).
- <sup>23</sup>Y. Li, W. Huang, H. Huang, C. Hewitt, Y. Chen, G. Fang, and D. L. Carroll. Evaluation of methods to extract parameters from current-voltage characteristics of solar cells. *Sol. Energy*, **90**, 51–57 (2013).
- <sup>24</sup>V. J. Chin, Z. Salam, and K. Ishaque. Cell modelling and model parameters estimation techniques for photovoltaic simulator application: A review. *Appl. Energy*, **154**, 500–519 (2015).
- <sup>25</sup>C Groves. Simulating charge transport in organic semiconductors and devices: a review. *Rep. Prog. Phys.*, **80**(2), 026502 (2016).
- <sup>26</sup>A. Raba, Y. Leroy, and A.-S. Cordan. Organic solar cells: a rigorous model of the donor-acceptor interface for various bulk heterojunction morphologies. *J. Appl. Phys.*, **115**(5), 054508 (2014).
- <sup>27</sup>Tektronix. Keithley series 2400 SourceMeter Datasheet, 2020. URL [https://download.tek.com/datasheet/1KW-2798-3\\_2400\\_SourceMeter\\_SMU\\_Datasheet\\_041121.pdf](https://download.tek.com/datasheet/1KW-2798-3_2400_SourceMeter_SMU_Datasheet_041121.pdf).
- <sup>28</sup>Rhode & Schwarz. RTM3000 Oscilloscope Datasheet, 2018. URL [https://www.batronix.com/files/Rohde-&-Schwarz/Oscilloscope/RTM3000/RTM3000\\_datasheet.pdf](https://www.batronix.com/files/Rohde-&-Schwarz/Oscilloscope/RTM3000/RTM3000_datasheet.pdf).
- <sup>29</sup>Agilent 4294A Precision Impedance Analyzer. URL <https://www.keysight.com/fr/en/assets/7018-06715/technical-overviews/5952-1430.pdf>.
- <sup>30</sup>COMSOL AB, COMSOL Multiphysics® Reference Manual, version 5.5, 2019.
- <sup>31</sup>David J. C. MacKay. *Information Theory, Inference, and Learning Algorithms*, page 640. Cambridge University Press, 2003.
- <sup>32</sup>J. Goodman and J. Wear. Ensemble samplers with affine invariance. *Comm. App. Math. Comp. Sci.*, **5**(1), 65–80 (2010).
- <sup>33</sup>D. Foreman-Mackey, D. W. Hogg, D. Lang, and J. Goodman. emcee: The MCMC Hammer. *Publ. Astron. Soc. Pac.*, **125**(925), 306–312 (2013). [arXiv:1202.3665](https://arxiv.org/abs/1202.3665).
- <sup>34</sup>K. Levenberg. A method for the solution of certain non-linear problems in least squares. *Q. Appl. Math.*, **2**(2), 164–168 (1944).
- <sup>35</sup>D. W. Marquardt. An algorithm for least-squares estimation of nonlinear parameters. *SIAM Rev. Soc. Ind. Appl. Math.*, **11**(2), 431–441 (1963).
- <sup>36</sup>J. J. Moré. The Levenberg-Marquardt Algorithm: Implementation and Theory. In *Numerical analysis*, pages 105–116. Springer, 1978.
- <sup>37</sup>M. C. Heiber, K. Kister, A. Baumann, V. Dyakonov, C. Deibel, and T.-Q. Nguyen. Impact of Tortuosity on Charge-Carrier Transport in Organic Bulk Heterojunction Blends. *Phys. Rev. Appl.*, **8**(5), 054043 (2017).
- <sup>38</sup>B. Ray, M. S. Lundstrom, and M. A. Alam. Can morphology tailoring improve the open circuit voltage of organic solar cells? *Appl. Phys. Lett.*, **100**(1), 013307 (2012).